Geophysical Research Letters

RESEARCH LETTER
10.1029/2023GL107009

Key Points:

- While seasonal variability dominates ENSO-related surface turbulent heat fluxes over the North Pacific, synoptic effects are non-negligible
- ENSO-related storm track shift affects the high-frequency contribution to the turbulent heat fluxes
- Differences in the bulk formula coefficient between two ENSO phases have a small but non-negligible influence on the surface heat fluxes

Supporting Information:

Supporting Information may be found in the online version of this article.

Correspondence to:
H.-H. Wei,
ho-hsuan.wei@noaa.gov

Citation:
Wei, H.-H., Alexander, M., & Newman, M. (2024). Impact of time scales on North Pacific surface turbulent heat fluxes driven by ENSO. *Geophysical Research Letters*, *51*, e2023GL107009. https://doi.org/10.1029/2023GL107009

Received 31 OCT 2023
Accepted 24 JAN 2024

Impact of Time Scales on North Pacific Surface Turbulent Heat Fluxes Driven by ENSO

Ho-Hsuan Wei[1,2], Michael Alexander[2], and Matthew Newman[2]

[1]Cooperative Institute for Research in Environmental Sciences, Boulder, CO, USA, [2]NOAA Physical Sciences Laboratory, Boulder, CO, USA

Abstract ENSO's atmospheric teleconnections drive anomalous North Pacific sea surface temperatures through changes in surface heat fluxes ("the atmospheric bridge"). Previous research focusing on the bridge as a seasonal phenomenon did not consider how ENSO-related changes in synoptic variability might also impact surface turbulent heat fluxes (STHF). In this study, we find that while well over half of ENSO's impact on STHF occurs on low-frequency (>8 days) time scales, up to 20% of its impact arises on high-frequency (<8 days) time scales, through changes in the covariance between surface wind speed and air-sea enthalpy difference that typically warms the ocean south of the storm track. During El Niño, the North Pacific storm track and its attendant sea surface warming shift southward, reducing warming of the central North Pacific ocean and thereby enhancing the bridge signal there. Additionally, changes in the bulk formula coefficients between ENSO phases drive STHF differences (5%–10%).

Plain Language Summary The El Niño-Southern Oscillation (ENSO) has global impacts through teleconnections, which can influence the underlying ocean via the "atmospheric bridge." The atmospheric bridge results in upward surface heat flux and colder sea surface temperature (SST) over the central North Pacific and downward surface heat flux and warmer SST along the coast of North America during El Niño winters. While previous research has studied the influence of longer timescale features on this bridge-related surface heat flux pattern, the corresponding impact of shorter timescale variability remains unexplored. We find that while longer timescales (>8 days) dominate, shorter timescale influence on the fluxes is non-negligible. Shorter timescale variability warms the ocean south of the track of North Pacific storms. This warming contribution shifts with the storm location between the two ENSO phases. While the resulting difference between ENSO phases is small, it is mostly aligned with the total surface turbulent heat flux (STHF) difference between El Niño and La Niña. Also, the bulk formula coefficients used to compute the fluxes vary, leading to 5%–10% of the STHF difference between ENSO phases. In summary, the contribution of shorter timescale variability and coefficient changes to the North Pacific bridge-related STHF is small but non-negligible.

1. Introduction

El Niño-Southern Oscillation (ENSO)-driven signals from the tropical Pacific can influence the extratropical oceans and other tropical ocean basins through global atmospheric teleconnections, known as the "atmospheric bridge" (e.g., Alexander et al., 2002). The bridge-related SST anomalies are mainly due to changes in the surface heat and momentum fluxes, caused by anomalous changes in the near-surface air temperature, humidity, and winds. A key feature driving these ENSO-driven changes over the North Pacific Ocean is the deepening of the Aleutian Low during boreal winter (e.g., Bjerknes, 1966; Trenberth et al., 1998). The deeper low leads to stronger wind speeds along its southern flank and the advection of warm moist air on its eastern side and cold dry air to its west. The resulting anomalous surface fluxes create anomalously cold water in the central North Pacific and warm water along the coast of North America (e.g., Pan & Oort, 1983).

While the atmospheric bridge over the North Pacific has been well-documented on monthly and longer timescales, the impact of North Pacific atmospheric variability changes driven by ENSO on synoptic timescales has received less attention. Previous studies have shown that the North Pacific jet stream tends to shift equatorward and eastward over the eastern North Pacific, becoming more zonally oriented, during El Niño winters (e.g., Winters et al., 2019). The North Pacific storm track, a dominant feature on synoptic timescales, is influenced by this jet stream shift during ENSO events (e.g., Seager et al., 2010). This suggests that synoptic variability might also play a role in generating an ENSO-related signal in North Pacific ocean temperatures.

The bridge-related SST pattern has been shown to be largely forced by ENSO-related changes in surface heat fluxes (e.g., Alexander, 1992). The surface heat flux difference between El Niño and La Niña winters (hereafter EN−LN) is dominated by the surface turbulent heat flux (STHF) over the North Pacific (Figure S1 in Supporting Information S1). The surface turbulent sensible heat flux (SHF) and latent heat flux (LHF) are generally estimated using bulk formula, which involve the product of transfer coefficients, wind speed, and air-sea temperature and moisture differences. Note that all three quantities vary on both high- and low-frequency time scales. This includes the coefficients, which have often been assumed to be constant in both time and space (e.g., Alexander & Scott, 1997; Gao et al., 2019), or alternatively variable in space but constant in time, determined through linear regression techniques (e.g., DeMott et al., 2016). Fixing the transfer coefficients in time can be helpful for focusing on the roles of wind speed and air-sea difference directly and provides simplicity for decomposition and computation. However, since the transfer coefficients are functions of near-surface wind speed and instability due to air-sea temperature difference, they vary both in time and space and therefore also impact STHF variability.

In this study, we define the "ENSO signal" as the difference between El Niño and La Niña winters (i.e., EN−LN) and examine how different timescales of near-surface quantities influence the ENSO signal in STHF over the North Pacific. In this analysis, we include the timescale impact on bulk coefficients, which we determine directly rather than from regression techniques. The data used in this study and the methods used to detect extratropical storms, decompose the STHF on different timescales, and compute the time-varying coefficients are described in Section 2. The results are presented in Section 3 and the conclusions in Section 4.

2. Data and Methodology

2.1. ERA5 Reanalysis

We examine 40 years (1979–2018) of boreal winter (December–February) single-level hourly data on a $0.25° \times 0.25°$ grid from ERA5, the fifth-generation atmospheric reanalysis of the European Centre for Medium-range Weather Forecasts (ECMWF) (Hersbach et al., 2020). STHF is calculated using analyzed SST, air and dew-point temperatures at 2 m, and the 10-m u and v wind.

2.2. Storm Track Detection Method

A storm track detection method based on sea level pressure is used for calculating storm composites and storm statistics. The algorithm, originally developed by Chelton et al. (2011) for tracking mesoscale ocean eddies, was modified by Oliver and Cavanagh (https://github.com/ecjoliver/stormTracking) for detecting and tracking extratropical cyclones. In the algorithm, the storms are detected first, and then are grouped into storm tracks based on criteria related to storm propagation speed, lifetime, and traveling distances. More details of the algorithm can be found from Chelton et al. (2011), the GitHub page, and in Supporting Information S1 (Text S1, including our modifications to the algorithm).

2.3. Decomposition of Surface Fluxes

The bulk formula for STHF is decomposed into terms composed of climatological, low-frequency, and high-frequency time scales (e.g., Newman et al., 2012; Wu et al., 2020). We use the *aerobulk-python* package (https://github.com/xgcm/aerobulk-python), a python wrapper for AeroBulk (Brodeau et al., 2017), to calculate the turbulent fluxes, SHF and LHF, as

$$\mathrm{SHF} = \rho C_p C_h U_b (\theta_{10m} - \theta_{\mathrm{sfc}}) = C_{\mathrm{SH}} U_b d\theta \tag{1}$$

$$\mathrm{LHF} = \rho L_v C_q U_b \left(q_{10m} - q_{s,\mathrm{sfc}}\right) = C_{\mathrm{LH}} U_b dq, \tag{2}$$

where ρ is the density of atmosphere, C_p the specific heat capacity at constant pressure, C_h the transfer coefficient for heat, U_b the bulk wind speed ($\sqrt{u_{10m}^2 + v_{10m}^2 + w_*^2}$, where w_* is the free convection velocity scale (ECMWF, 2016)), θ_{10m} the 10-m potential temperature, θ_{sfc} the surface potential temperature, L_v the latent heat of vaporization, C_q the transfer coefficient for moisture, q_{10m} the 10-m specific humidity, $q_{s,\mathrm{sfc}}$ the surface saturated specific humidity, $C_{\mathrm{SH}} = \rho C_p C_h$, $C_{\mathrm{LH}} = \rho L_v C_q$, $d\theta = \theta_{10m} - \theta_{\mathrm{sfc}}$, and $dq = q_{10m} - q_{s,\mathrm{sfc}}$. The θ_{10m} and q_{10m} are derived from the 2-m quantities. The right and left sides of Equations 1 and 2 were not identical when computed

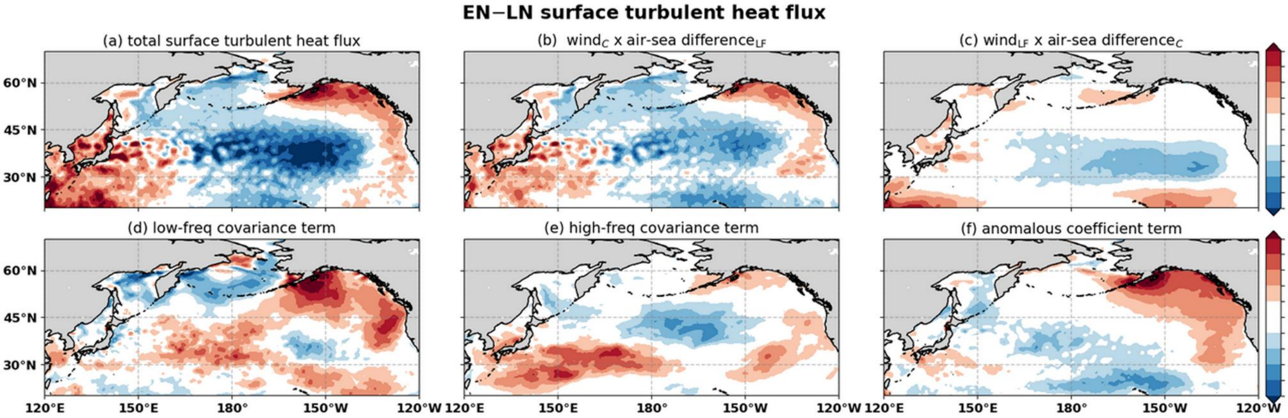

Figure 1. The EN−LN (a) total STHF $\left(\overline{\mathrm{SHF}+\mathrm{LHF}}^{\mathrm{EN-LN}}\right)$ and the terms on the right side of the sum of Equations 3 and 4: (b) the interaction between DJF climatological wind speed and low-frequency air-sea enthalpy difference $\left(\overline{C_{\mathrm{SH}_C} U_{b_C} d\theta_{\mathrm{LF}} + C_{\mathrm{LH}_C} U_{b_C} dq_{\mathrm{LF}}}^{\mathrm{EN-LN}}\right)$, (c) the interaction between low-frequency wind speed and DJF climatological air-sea enthalpy difference $\left(\overline{C_{\mathrm{SH}_C} U_{b_{\mathrm{LF}}} d\theta_C + C_{\mathrm{LH}_C} U_{b_{\mathrm{LF}}} dq_C}^{\mathrm{EN-LN}}\right)$, (d) the low-frequency covariance term $(\overline{C_{\mathrm{SH}_C} U_{b_{\mathrm{LF}}} d\theta_{\mathrm{LF}} + C_{\mathrm{LH}_C} U_{b_{\mathrm{LF}}} dq_{\mathrm{LF}}}^{\mathrm{EN-LN}})$, (e) the high-frequency covariance term $(\overline{C_{\mathrm{SH}_C} U_{b_{\mathrm{HF}}} d\theta_{\mathrm{HF}} + C_{\mathrm{LH}_C} U_{b_{\mathrm{HF}}} dq_{\mathrm{HF}}}^{\mathrm{EN-LN}})$, and (f) the anomalous coefficient term $\left(\overline{C_{\mathrm{SH}_{\mathrm{ANO}}} U_b d\theta + C_{\mathrm{LH}_{\mathrm{ANO}}} U_b dq}^{\mathrm{EN-LN}}\right)$. Subscript C represents climatology, LF low-frequency, HF high-frequency, and ANO anomaly. The units are W m^{-2}. Notice that the colorbar ranges are (a–c) −40 to 40 and (d–f) −5 to 5 W m^{-2}.

from the archived ERA5 output values, so both fluxes (defined as positive when heating the ocean) are calculated using the aerobulk-python package based on the ECMWF parameterization; the computed STHF values are similar to those from ERA5. Since we compute the fluxes rather than take them directly from the reanalysis, the left and right side of Equations 1 and 2, as well as their full decomposition given below are equal.

To separate the contributions of synoptic versus longer timescales, the right-hand side terms of Equations 1 and 2 are recomputed after decomposing each variable (C_{SH}, C_{LH}, U_b, $d\theta$, and dq) into its climatology (C) (defined by the first four annual harmonics), low-frequency (LF) component (periods > 8 days), and high-frequency (HF) component (periods < 8 days). Note that while the coefficients are a function of wind speed and stability (air-sea temperature difference), we did not decompose C_{SH} and C_{LH} using these variables since they are highly nonlinear. Instead, the time series of the coefficients are decomposed into C, LF, and HF directly. Additionally, we decompose the wind speed rather than the vector wind, since the STHF is a function of the former.

The SHF and LHF become:

$$\mathrm{SHF} = \left(C_{\mathrm{SH}_C} + C_{\mathrm{SH}_{\mathrm{LF}}} + C_{\mathrm{SH}_{\mathrm{HF}}}\right)\left(U_{b_C} + U_{b_{\mathrm{LF}}} + U_{b_{\mathrm{HF}}}\right)\left(d\theta_C + d\theta_{\mathrm{LF}} + d\theta_{\mathrm{HF}}\right)$$
$$\mathrm{LHF} = \left(C_{\mathrm{LH}_C} + C_{\mathrm{LH}_{\mathrm{LF}}} + C_{\mathrm{LH}_{\mathrm{HF}}}\right)\left(U_{b_C} + U_{b_{\mathrm{LF}}} + U_{b_{\mathrm{HF}}}\right)\left(dq_C + dq_{\mathrm{LF}} + dq_{\mathrm{HF}}\right).$$

This leads to nine terms that focus on the contribution of different timescales of U_b and $d\theta$ or dq, multiplied by the fixed climatological coefficient. The remaining 18 terms are combined into the "anomalous coefficient term" (e.g., $C_{\mathrm{SH}_{\mathrm{ANO}}} U_b d\theta$), where the total wind and air-sea temperature/moisture difference ($U_b d\theta$ or $U_b dq$) is multiplied by the sum of the anomalous (ANO) coefficients ($C_{\mathrm{SH}_{\mathrm{ANO}}} = C_{\mathrm{SH}_{\mathrm{LF}}} + C_{\mathrm{SH}_{\mathrm{HF}}}$ or $C_{\mathrm{LH}_{\mathrm{ANO}}} = C_{\mathrm{LH}_{\mathrm{LF}}} + C_{\mathrm{LH}_{\mathrm{HF}}}$).

To examine the flux components related to the atmospheric bridge, we calculate the EN−LN difference for each of the above terms. In the remainder of the paper, we discuss only the five terms that are found to be non-negligible, which are shown in Figure 1:

$$\overline{\mathrm{SHF}}^{\mathrm{EN-LN}} = \overline{\left[C_{\mathrm{SH}_C} U_{b_C} d\theta_{\mathrm{LF}} + C_{\mathrm{SH}_C} U_{b_{\mathrm{LF}}} d\theta_C + C_{\mathrm{SH}_C} U_{b_{\mathrm{LF}}} d\theta_{\mathrm{LF}} + C_{\mathrm{SH}_C} U_{b_{\mathrm{HF}}} d\theta_{\mathrm{HF}}\right]} \\ \overline{+\left[C_{\mathrm{SH}_{\mathrm{ANO}}} U_b d\theta\right]}^{\mathrm{EN-LN}} \tag{3}$$

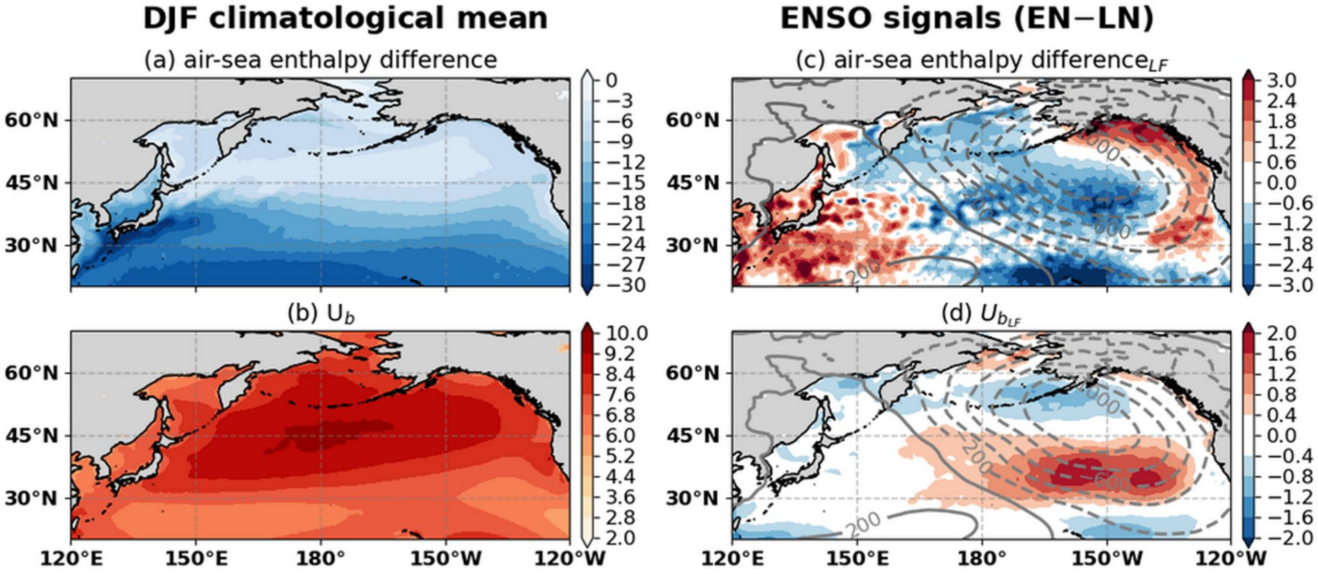

Figure 2. The DJF climatological mean of (a) the air-sea enthalpy difference ($C_{\mathrm{SH}_C} d\theta_{\mathrm{C}} + C_{\mathrm{LH}_C} dq_{\mathrm{C}}$, J m^{-3}) and (b) the surface bulk wind speed (U_{b_C}, m s^{-1}) and the EN−LN (c) low-frequency air-sea enthalpy difference ($\overline{C_{\mathrm{SH}_C} d\theta_{\mathrm{LF}} + C_{\mathrm{LH}_C} dq_{\mathrm{LF}}}^{\mathrm{EN-LN}}$, J m^{-3}) and (d) surface bulk wind speed ($\overline{U_{b_{\mathrm{LF}}}}^{\mathrm{EN-LN}}$, m s^{-1}). The contours in (c), (d) show the EN−LN sea level pressure (Pa), with contour interval as 200 Pa.

$$\overline{\mathrm{LHF}}^{\mathrm{EN-LN}} = \overline{\left[C_{\mathrm{LH}_C} U_{b_C} dq_{\mathrm{LF}} + C_{\mathrm{LH}_C} U_{b_{\mathrm{LF}}} dq_C + C_{\mathrm{LH}_C} U_{b_{\mathrm{LF}}} dq_{\mathrm{LF}} + C_{\mathrm{LH}_C} U_{b_{\mathrm{HF}}} dq_{\mathrm{HF}}\right] + \left[C_{\mathrm{LH}_{\mathrm{ANO}}} U_b dq\right]}^{\mathrm{EN-LN}} \tag{4}$$

where the $\overline{(\cdot)}^{\mathrm{EN-LN}} = \overline{(\cdot)}^{\mathrm{EN}} - \overline{(\cdot)}^{\mathrm{LN}}$, with $\overline{(\cdot)}^{\mathrm{EN}}$ the average over El Niño winters and $\overline{(\cdot)}^{\mathrm{LN}}$ the average over La Niña winters. The first two terms on the right side of Equations 3 and 4 are due to the interaction between climatological and low-frequency quantities. The third and fourth terms on the right side of Equations 3 and 4 are the LF and HF covariance terms, respectively. The last term is the anomalous coefficient term, which results from time-varying transfer coefficients. Analyses in this study are shown for the sum of SHF and LHF. For simplicity, we call $C_{\mathrm{SH}} d\theta + C_{\mathrm{LH}} dq$ the air-sea enthalpy difference. Focusing on the air-sea enthalpy difference ($\rho C_e C_p d\theta$ and $\rho C_q L_v dq$), rather than the air-sea temperature and moisture differences ($d\theta$ and dq), allows us to consider the combined effects of the SHF and LHF.

3. Results

The STHF ENSO signal has upward fluxes (negative values of EN−LN) over the central North Pacific and downward fluxes (positive values of EN−LN) along the coast of North America (Figure 1a), matching the bridge-related SST pattern and consistent with previous studies (e.g., Alexander et al., 2002; Pan & Oort, 1983). After decomposing the fluxes, we found that the interaction between climatological and low-frequency quantities (first two terms on the right side of Equations 3 and 4; Figures 1b and 1c) dominates the total EN−LN difference in STHF (Figure 1a), with as much as half of its magnitude in some regions. The other three terms (LF and HF covariance, and the anomalous coefficient term, Figures 1d–1f) are relatively small ($\leq$5 W m^{-2}), but are non-negligible since they each contribute as much as ~20%–25% of the total EN−LN STHF in some regions.

The patterns of the two dominant terms (Figures 1b and 1c) are mainly determined by the patterns of the low-frequency atmospheric response to ENSO. The first dominant term (Figure 1b) is approximately equal to U_{b_C} (Figure 2b) times $\overline{C_{\mathrm{SH}_C} d\theta_{\mathrm{LF}} + C_{\mathrm{LH}_C} dq_{\mathrm{LF}}}^{\mathrm{EN-LN}}$ (Figure 2c), and the second (Figure 1c) is approximately equal to $C_{\mathrm{SH}_C} d\theta_{\mathrm{C}} + C_{\mathrm{LH}_C} dq_{\mathrm{C}}$ (Figure 2a) times $\overline{U_{b_{\mathrm{LF}}}}^{\mathrm{EN-LN}}$ (Figure 2d). Both terms are a consequence of the deepened Aleutian Low during El Niño relative to La Niña (contours in Figures 2c and 2d). For the first term, the stronger low circulation drives enhanced advection that makes the near-surface atmosphere warmer and moister (colder and dryer) to the east and north (west and south) of the low center. The resulting EN−LN $\theta_{10\mathrm{m}}$ and $q_{10\mathrm{m}}$ anomalies

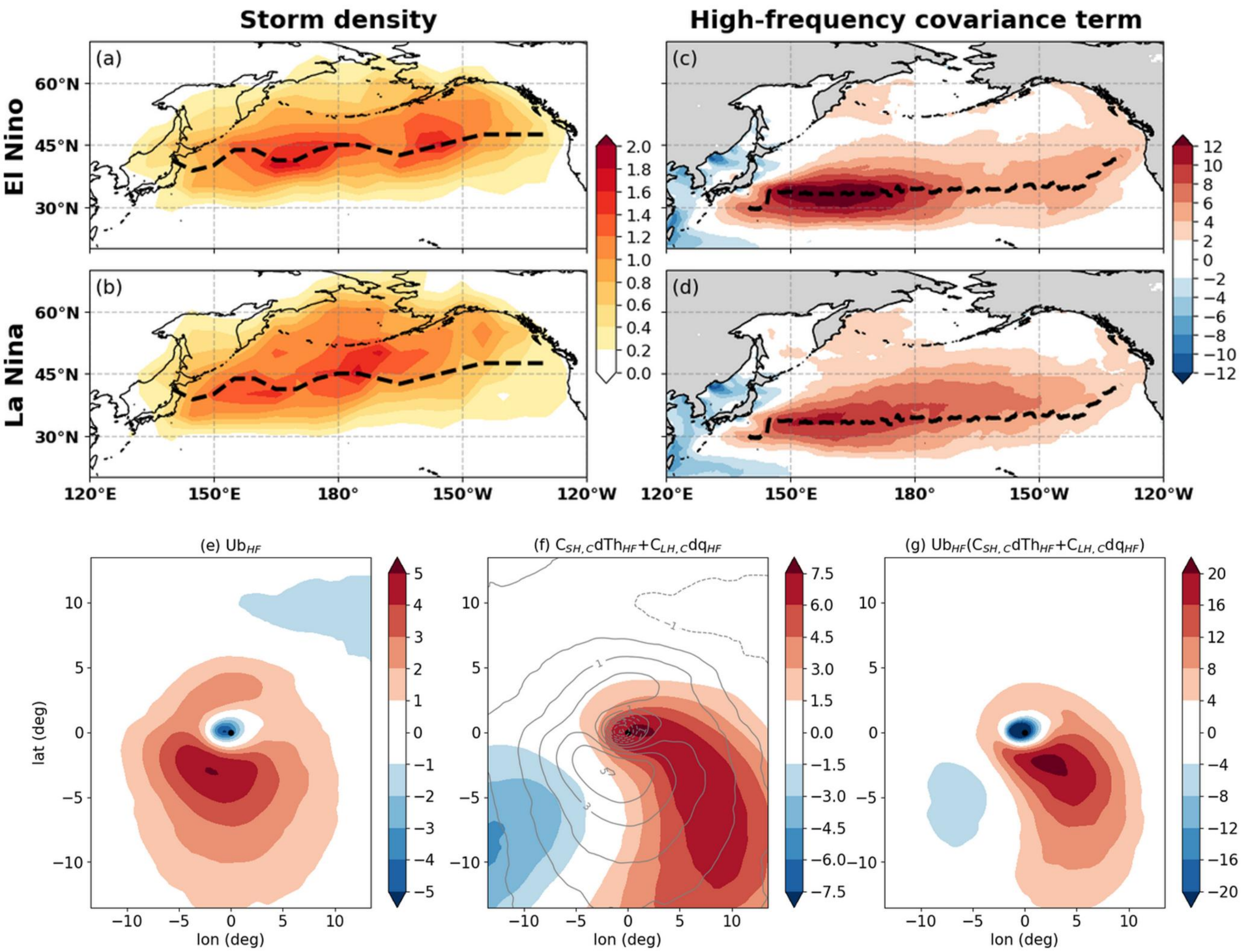

Figure 3. The storm density (number per month) within 5-degree × 5-degree grid boxes over (a) El Niño and (b) La Niña winters (DJF). (c, d) Same as (a, b) except for the HF covariance term (W m^{-2}). The smoothed location of maximum El Niño storm density in meridional direction (between 140°E and 130°W) are shown as black dashed lines (in both (a) and (b)). Black dashed Lines in (c), (d) are similar as the ones in (a), (b) but for HF covariance term. The storm composite of HF (e) U_b (m s^{-1}), (f) air-sea enthalpy difference (J m^{-3}), and (g) the multiplication of the (e) and (f) (W m^{-2}) for the storms located within 42.5–47.5°N and 175°E–175°W. The contours in (f) are the HF U_b shown in (e).

correspond to EN−LN low-frequency $d\theta$ (i.e., $\theta_{10m} - \theta_{sfc}$) and dq (i.e., $q_{10m} - q_{s,sfc}$) and same-signed EN−LN air-sea enthalpy difference (Figure 2c). Additionally, the deeper Aleutian Low drives intensified surface westerlies south of the low center (contours in Figure 2c), so that the total wind speed increases over the region 30–45° N, 180–130°W. This creates a positive EN−LN difference in low-frequency surface wind speed (Figure 2d) that acts to cool the ocean Figure 1c.

During El Niño, the wintertime North Pacific storm track tends to be more zonally oriented than during La Niña, with increased storm density located both more eastward and more equatorward especially over the eastern North Pacific (Figures 3a and 3b; Figure S3 in Supporting Information S1). This shift in the storm track's location and strength is the principal driver of changes in the HF contribution to the EN−LN STHF shown in Figure 1e. The HF covariance term (Figures 3c and 3d) tends to be positive south of the storm track, with a maximum in the western Pacific, during both El Niño and La Niña. That is, the HF covariance term warms the ocean on the equatorward side of the storm track. Since the storm track shifts southward and eastward during El Niño relative to La Niña (cf. Figures 3a and 3b; note that the black dashed line indicates the El Niño storm track position in both figures), the corresponding positive HF covariance term shifts accordingly (cf. Figures 3c and 3d). This leads to the ENSO-related difference of the HF covariance term (Figure 1e), with negative EN−LN values over the central

10.1029/2023GL107009

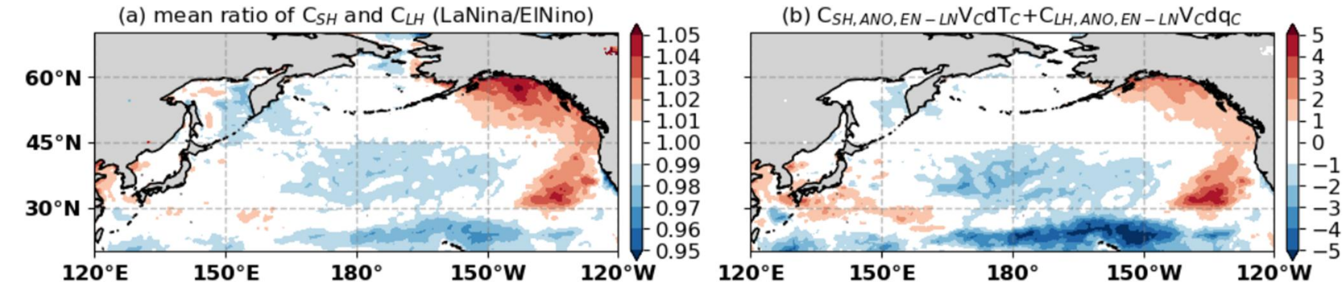

Figure 4. (a) The mean ratio of the coefficient for SHF and LHF between La Niña and El Niño (i.e., mean of $C_{SH_{LN}}/C_{SH_{EN}}$ and $C_{LH_{LN}}/C_{LH_{EN}}$). The values larger than one (red shading) indicate that the coefficient in La Niña years is larger. (b) The EN−LN bulk formula coefficient multiplies the climatological wind speed and air-sea difference ($\overline{C_{SH_{ANO}}}^{EN-LN} U_{b_C} d\theta_C + \overline{C_{LH_{ANO}}}^{EN-LN} U_{b_C} dq_C$, W m^{-2}).

North Pacific and positive EN−LN values near the west coast of North America, reinforcing the pattern of total EN−LN STHF (Figure 1a).

Asymmetries within the extratropical cyclones act to drive the ENSO-related storm track contribution to STHF. This is diagnosed using a storm-centric composite (Figures 3e–3g), which allows the HF covariance term to be decomposed into its different components. HF U_b is generally positive around the storm center with relatively larger U_b to the south of the low center (Figure 3e). The warm sector can be identified in the HF air-sea enthalpy difference (Figure 3f), which is closely related to the HF air temperature and moisture because SST and the corresponding q_s have relatively smaller HF variability. Northward advection of warm moist air within the warm sector leads to higher near-surface atmospheric T and q, resulting in positive HF $d\theta$ and dq (Figure 3f). Conversely, advection of cold dry air behind the cold front yields a negative HF air-sea enthalpy difference there that is somewhat weaker and less spatially extensive (Figure 3f). This warm/cold sector asymmetry in HF air-sea enthalpy difference is related to the "lateral mixing" explanation of poleward moisture transport by synoptic eddies (e.g., Newman et al., 2012): Since the storm track is located north of the region of strong moisture gradient (Figure S2b in Supporting Information S1), overall meridional moisture transport is dominated by down-gradient moisture advection within the warm sector, whereas much weaker moisture gradient leads to weaker moisture transport in the cold sector. Similar but weaker asymmetry is seen in thermal advection (Figure S2a in Supporting Information S1) so that the air-sea enthalpy difference is much larger in the warm sector.

The asymmetry in location between the positive and negative air-sea enthalpy difference (Figure 3f) is typical of mature extratropical storms: the warm sector tends to be located closer to the center of the storm, associated with stronger winds due to a strong pressure gradient and reduced low-level stability, while the cold sector is located further away behind the cold front where the pressure gradient is weaker, low-level stability is enhanced, and winds are weaker (Martin, 1998; Schultz & Vaughan, 2011; Schultz et al., 2019). Consequently, the region of positive $d\theta$ and dq values in the warm sector is associated with much stronger HF wind speeds than is the region of negative $d\theta$ and dq in the cold sector (Figure 3f). These asymmetries lead to stronger positive covariance in the warm sector and smaller negative covariance in the cold sector (Figure 3g), so that the net covariance between HF U_b and air-sea enthalpy differences, averaged over all extratropical cyclones, is positive to the south of the storm track (Figures 3a–3d).

Both HF and LF variability in surface wind speed and low-level stability lead to variability in the bulk formula coefficients used to determine SHF and LHF. Consequently, there are also ENSO signals in these coefficients given by the last term of Equations 3 and 4 (shown in Figure 1f). The ratio of the coefficients can differ by as much as 5% between EN and LN (Figure 4a). This pattern is similar to the EN−LN air-sea enthalpy difference (Figure 2c), which can be treated as an estimate of near-surface instability since it is similar to $d\theta$ (Figure S4 in Supporting Information S1). The pattern of the coefficient ratio is like the pattern of EN−LN instability, with more positive $d\theta$ (more stable) corresponding to smaller coefficients (Figure S4 in Supporting Information S1; Figure 4a). For example, the EN−LN stability is positive along the west coast of North America (Figure S4 in Supporting Information S1), which corresponds to smaller coefficients (Figure 4a) and more downward surface fluxes during El Niño (positive EN−LN anomalous coefficient term in Figure 1f). While the EN−LN U_b (cf. Figure 2d) also influences the coefficients, its pattern does not resemble the EN−LN coefficient (Figure 4a).

However, since the coefficient has a nonlinear dependence on both wind speed and instability, it is difficult to entirely separate the impact of U_b and $d\theta$ on the coefficient values.

To quantify how the ENSO signals in the coefficients directly contribute to the EN−LN total STHF, we calculate the product of the EN−LN coefficient and climatological U_b and $d\theta$ (and dq) (Figure 4b). This is the dominant component of the full anomalous coefficient term (Figure 1f) except for the area south of Alaska.

4. Discussion and Conclusion

While previous studies have examined the atmospheric bridge to the North Pacific on monthly and longer timescales, the role of high-frequency variability, particularly within the STHF, has not been well-studied. The jet stream and storm track tend to shift southward and eastward during El Niño winters over the eastern North Pacific, which has the potential to influence surface fluxes on synoptic timescales. We found that while the low-frequency features dominate the ENSO signals in STHF, the high-frequency features still play a non-negligible role through the HF covariance term $\left(\overline{C_{\mathrm{SH}_C} U_{b_{\mathrm{HF}}} d\theta_{\mathrm{HF}} + C_{\mathrm{LH}_C} U_{b_{\mathrm{HF}}} dq_{\mathrm{HF}}}^{\mathrm{EN-LN}}\right)$. This HF covariance term is positive slightly south of the storm track due to the asymmetry of the covariance of wind speed and air-sea enthalpy difference between the warm and cold sectors of extratropical storms. Due to the ENSO-related shift of the storm track, this positive HF covariance term also shifts and exhibits a similar pattern as the EN−LN total STHF, which can contribute up to 20% of the EN−LN total STHF in some locations.

We also examined how changes in the bulk formula coefficients influence the EN−LN STHF. The ENSO signals in the anomalous coefficient term contribute up to around 5%–10% of the EN−LN total STHF near the coast of North America (Figure 4b). The coefficients have a nonlinear dependence on both instability ($d\theta$) and wind speed (U_b), with a wide range in values, making it difficult to separate the effects of the two variables on the coefficient values.

While the cooling of the ocean is normally observed after storm-passing, the HF covariance term here seems to show a counter-intuitive result that the storm warms the ocean to the equatorward side of the storm tracks, which is a result that is not dependent on the state of ENSO (Figures 3c and 3d). One of the possible reasons is that, here, we only evaluated the STHF as a function of time scale. The SST tendency, however, can be also influenced by many other processes. For example, both mixing in the ocean triggered by wind stirring and buoyancy forcing at the surface, and Ekman heat transport can also change the bridge-related SST (Alexander, 1992; Alexander & Scott, 2008; Alexander et al., 2002), and vary on synoptic timescales. More research is needed to understand the relative contribution of these different processes.

Also, time-filtering wind speed can lead to different cut-off timescales compared to filtering wind vectors, resulting in different results. Synoptic timescale features also influence other atmospheric bridge processes, for example, the atmospheric energy transport (e.g., Mayer & Haimberger, 2012; Trenberth & Caron, 2001). Quantifying how these and other high-frequency processes can influence ENSO-driven SST differences requires further analysis.

Data Availability Statement

The hourly ERA5 reanalysis data was downloaded from Copernicus Climate Change Service (C3S) Data Store (CDS) (Hersbach et al., 2017). The storm track detection package was downloaded from https://github.com/ecjoliver/stormTracking.

Acknowledgments
This work was supported by NOAA cooperative agreements NA17OAR4320101 and NA22OAR4320151. The lead author wants to thank Sang-Ik Shin, Pragallva Barpanda, and Chia-Wei Hsu for their helpful discussion and suggestions.

References

Alexander, M. A. (1992). Midlatitude atmosphere–ocean interaction during El Niño. Part I: The North Pacific ocean. *Journal of Climate*, *5*(9), 944–958. https://doi.org/10.1175/1520-0442(1992)005<0944:maiden>2.0.co;2

Alexander, M. A., Bladé, I., Newman, M., Lanzante, J. R., Lau, N.-C., & Scott, J. D. (2002). The atmospheric bridge: The influence of ENSO teleconnections on air–sea interaction over the global oceans. *Journal of Climate*, *15*(16), 2205–2231. https://doi.org/10.1175/1520-0442(2002)015⟨2205:TABTIO⟩2.0.CO;2

Alexander, M. A., & Scott, J. D. (1997). Surface flux variability over the North Pacific and North Atlantic oceans. *Journal of Climate*, *10*(11), 2963–2978. https://doi.org/10.1175/1520-0442(1997)010⟨2963:SFVOTN⟩2.0.CO;2

Alexander, M. A., & Scott, J. D. (2008). The role of Ekman ocean heat transport in the Northern Hemisphere response to ENSO. *Journal of Climate*, *21*(21), 5688–5707. https://doi.org/10.1175/2008JCLI2382.1

Bjerknes, J. (1966). A possible response of the atmospheric Hadley circulation to equatorial anomalies of ocean temperature. *Tellus*, *18*(4), 820–829. https://doi.org/10.3402/tellusa.v18i4.9712

Brodeau, L., Barnier, B., Gulev, S. K., & Woods, C. (2017). Climatologically significant effects of some approximations in the bulk parameterizations of turbulent air–sea fluxes. *Journal of Physical Oceanography*, *47*(1), 5–28. https://doi.org/10.1175/JPO-D-16-0169.1

Chelton, D. B., Schlax, M. G., & Samelson, R. M. (2011). Global observations of nonlinear mesoscale eddies. *Progress in Oceanography*, *91*(2), 167–216. https://doi.org/10.1016/j.pocean.2011.01.002

DeMott, C. A., Benedict, J. J., Klingaman, N. P., Woolnough, S. J., & Randall, D. A. (2016). Diagnosing ocean feedbacks to the MJO: SST-modulated surface fluxes and the moist static energy budget. *Journal of Geophysical Research: Atmospheres*, *121*(14), 8350–8373. https://doi.org/10.1002/2016JD025098

ECMWF. (2016). IFS documentation CY41R2—Part IV: Physical processes. https://doi.org/10.21957/tr5rv27xu

Gao, Y., Hsu, P.-C., & Li, T. (2019). Effects of high-frequency activity on latent heat flux of MJO. *Climate Dynamics*, *52*(3–4), 1471–1485. https://doi.org/10.1007/s00382-018-4208-1

Hersbach, H., Bell, B., Berrisford, P., Hirahara, S., Horányi, A., Muñoz-Sabater, J., et al. (2020). The ERA5 global reanalysis. *Quarterly Journal of the Royal Meteorological Society*, *146*(730), 1999–2049. https://doi.org/10.1002/qj.3803

Hersbach, H., Bell, B., Berrisford, P., Hirahara, S., Horányi, A., Muñoz-Sabater, J., et al. (2017). Complete ERA5 from 1940: Fifth generation of ECMWF atmospheric reanalyses of the global climate [Dataset]. Copernicus Climate Change Service (C3S) Data Store (CDS). https://doi.org/10.24381/cds.143582cf

Martin, J. E. (1998). The structure and evolution of a continental winter cyclone. Part I: Frontal structure and the occlusion process. *Monthly Weather Review*, *126*(2), 303–328. https://doi.org/10.1175/1520-0493(1998)126⟨0303:TSAEOA⟩2.0.CO;2

Mayer, M., & Haimberger, L. (2012). Poleward atmospheric energy transports and their variability as evaluated from ECMWF reanalysis data. *Journal of Climate*, *25*(2), 734–752. https://doi.org/10.1175/JCLI-D-11-00202.1

Newman, M., Kiladis, G. N., Weickmann, K. M., Ralph, F. M., & Sardeshmukh, P. D. (2012). Relative contributions of synoptic and low-frequency eddies to time-mean atmospheric moisture transport, including the role of atmospheric rivers. *Journal of Climate*, *25*(21), 7341–7361. https://doi.org/10.1175/JCLI-D-11-00665.1

Pan, Y. H., & Oort, A. H. (1983). Global climate variations connected with sea surface temperature anomalies in the eastern equatorial Pacific Ocean for the 1958–73 period. *Monthly Weather Review*, *111*(6), 1244–1258. https://doi.org/10.1175/1520-0493(1983)111⟨1244:GCVCWS⟩2.0.CO;2

Schultz, D. M., Bosart, L. F., Colle, B. A., Davies, H. C., Dearden, C., Keyser, D., et al. (2019). Extratropical cyclones: A century of research on meteorology's centerpiece. *Meteorological Monographs*, *59*, 16.1–16.56. https://doi.org/10.1175/AMSMONOGRAPHS-D-18-0015.1

Schultz, D. M., & Vaughan, G. (2011). Occluded fronts and the occlusion process: A fresh look at conventional wisdom. *Bulletin of the American Meteorological Society*, *92*(4), 443–466. https://doi.org/10.1175/2010BAMS3057.1

Seager, R., Naik, N., Ting, M., Cane, M. A., Harnik, N., & Kushnir, Y. (2010). Adjustment of the atmospheric circulation to tropical Pacific SST anomalies: Variability of transient eddy propagation in the Pacific–North America sector. *Quarterly Journal of the Royal Meteorological Society*, *136*(647), 277–296. https://doi.org/10.1002/qj.588

Trenberth, K. E., Branstator, G. W., Karoly, D., Kumar, A., Lau, N.-C., & Ropelewski, C. (1998). Progress during toga in understanding and modeling global teleconnections associated with tropical sea surface temperatures. *Journal of Geophysical Research*, *103*(C7), 14291–14324. https://doi.org/10.1029/97JC01444

Trenberth, K. E., & Caron, J. M. (2001). Estimates of meridional atmosphere and ocean heat transports. *Journal of Climate*, *14*(16), 3433–3443. https://doi.org/10.1175/1520-0442(2001)014⟨3433:EOMAAO⟩2.0.CO;2

Winters, A. C., Keyser, D., & Bosart, L. F. (2019). The development of the North Pacific jet phase diagram as an objective tool to monitor the state and forecast skill of the upper-tropospheric flow pattern. *Weather and Forecasting*, *34*(1), 199–219. https://doi.org/10.1175/WAF-D-18-0106.1

Wu, R., Jiao, Y., Wang, Y., & Jia, X. (2020). High-frequency wind-related seasonal mean latent heat flux changes over the tropical Indo-western Pacific in El Niño and La Niña years. *Journal of Geophysical Research: Atmospheres*, *125*(21), e2020JD032954. https://doi.org/10.1029/2020JD032954

References From the Supporting Information

Klotzbach, P. J., Oliver, E. C., Leeper, R. D., & Schreck, C. J. (2016). The relationship between the Madden–Julian oscillation (MJO) and southeastern New England snowfall. *Monthly Weather Review*, *144*(4), 1355–1362. https://doi.org/10.1175/MWR-D-15-0434.1